# Supplementary Information: Interlayer exciton landscape in $WS_2$/tetracene heterostructures

Joshua J. P. Thompson,[1] Victoria Lumsargis,[2] Maja Feierabend,[3] Quichen Zhao,[2,4] Kang Wang,[5] Letian Dou,[5] Libai Huang,[2] and Ermin Malic[1,3]

[1]*Department of Physics, Philipps-Universität Marburg, 35037 Marburg, Germany*
[2]*Department of Chemistry, Purdue University, West Lafayette, Indiana, 47907, United States*
[3]*Department of Physics, Chalmers University of Technology, 412 96 Gothenburg, Sweden*
[4]*State Key Laboratory of Superhard Materials, Jilin University, Changchun, Jilin, 130012, China*
[5]*Davidson School of Chemical Engineering, Purdue University, West Lafayette, Indiana, 47907, United States*

## I. PREPARATION OF TUNGSTEN DISULFIDE/TETRACENE HETEROSTRUCTURE

### A. Tungsten disulfide preparation

The silicon dioxide wafer (oxide thickness of 90 nm) was cleaned in a sonication bath. The wafers were first sonicated in acetone, then isopropyl alcohol and finally deionized water for five minutes each. Bulk tungsten disulfide ($WS_2$) crystals (purchased from Graphene Supermarket) were then exfoliated onto the cleaned wafer using Scotch Magic Tape. Before lifting off the tape from the wafer, the bulk crystal taped to the silicon wafer was annealed on a hot plate at 100°C for two minutes [1]. The monolayer of $WS_2$ was found on the substrate using an Olympus Fluorescence Microscope. Optical images of the monolayer are shown in Fig. S1 (a). A mercury lamp was used to excite the monolayer which is shown in red in Figure S1 (a) ii. The room-temperature PL spectra (447 nm excitation) of the monolayer, heterostructure and pure tetracene (Tc) used in this study is shown in Fig. S1 (b). The single, narrow KK exciton peak at 2.0 eV is indicative that the $WS_2$ flake is a monolayer. The inset in Fig. S1 (b) is an enlargement of the spectra between 1.4-2.0 eV.

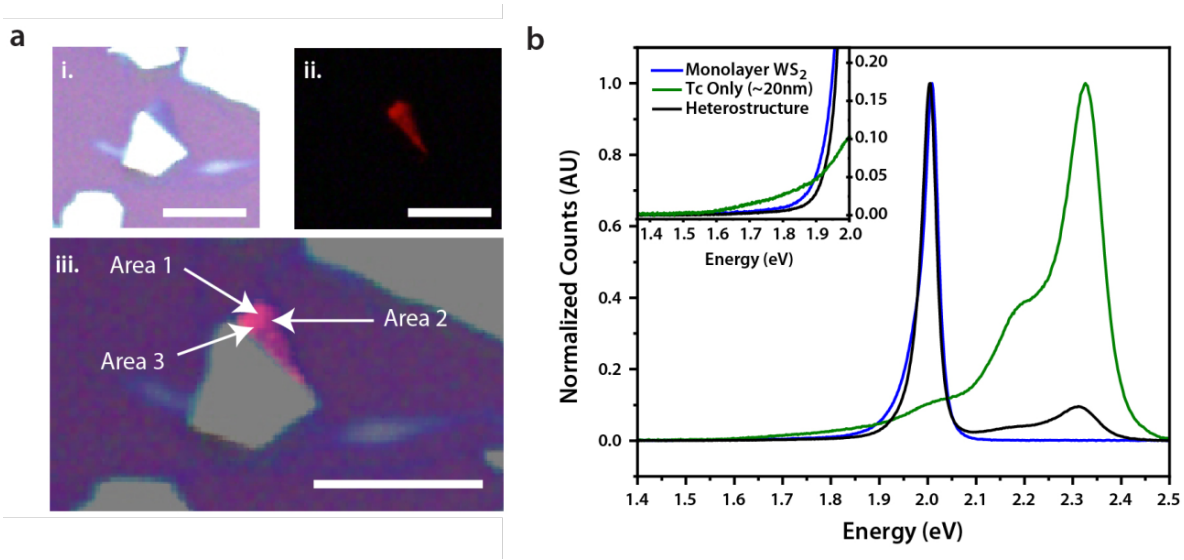


Figure S1. Characterization of $WS_2$, Tc and the heterostructure. (a) Optical Images of (i) the exfoliated monolayer of $WS_2$ (ii) the monolayer being excited with a mercury lamp (iii) the overlay of images (i) and (ii). The scale bar is 10 $\mu$m, while the PL areas of the different measurements are indicated with the white arrows. (b) the PL spectra of monolayer $WS_2$, pure Tc and the heterostructure when excited with 447 nm light. The inset in (b) is an enlargement of the main spectra between 1.4-2.0 eV.

### B. Tetracene Evaporation

Tetracene (98% ACROS Organics) was then thermally evaporated onto the sample using a LC Technology thermal evaporator with an INFICON (SQC-310) deposition controller. The tetracene was deposited at a rate of 0.5Å/s under a vacuum of $< 2$ x $10^{-6}$ mbar. The Tc height was measured using a Veeco Dimension 3100 Atomic Force Microscope (AFM). The AFM image in Fig. S2 shows two profiles which were used to determine a Tc thickness of $\sim 20$ nm.

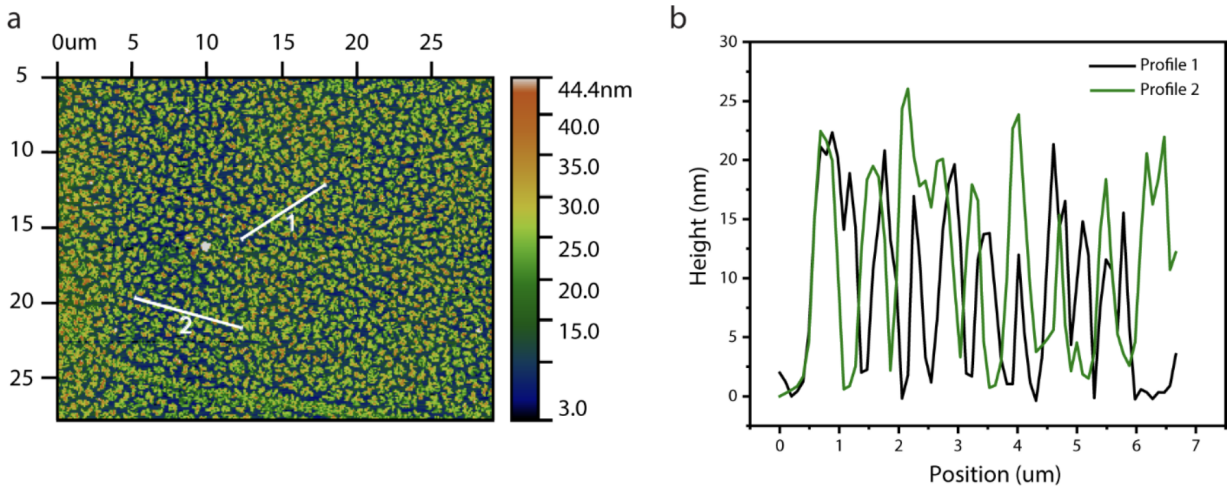


Figure S2. AFM of Tc. (a) AFM image of pure Tc showing the location of the two profiles plotted in (b).

X-ray diffraction (XRD) spectra of freshly evaporated Tc and a blank $SiO_2$/Si wafer is included in Fig. S3. The $2\theta$ peak in the Tc spectrum at 7.26° is in good agreement with XRD spectrum of a polymorph Tc thin film reported by Arias, D. et al. [2].

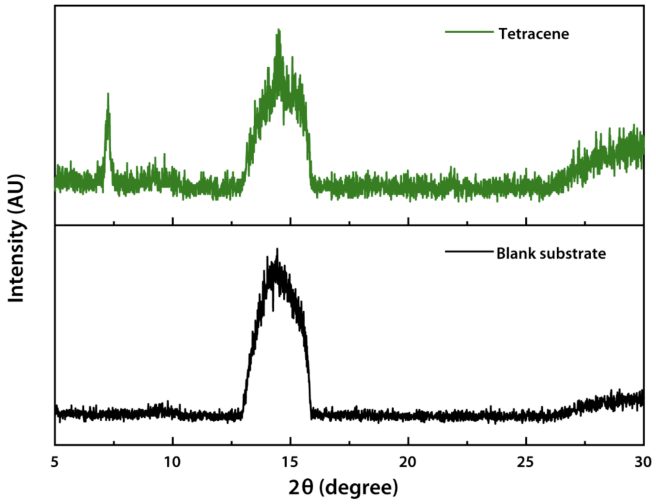


Figure S3. Figure S3. XRD spectra of (top) Tc and (bottom) $SiO_2$/Si.

During all PL measurements, the Tc remained as a thin film on the monolayer surface. However, after the course of approximately four months, the Tc's morphology changed into distinguishable crystals both on the $WS_2$ and $SiO_2$/Si surfaces.

## II. LOW-TEMPERATURE PHOTOLUMINESCENCE MEASUREMENTS

To measure the low temperature spectra of the heterostructure, the sample was cooled using a Montana Instrument Cryostation s50 (temperature stability $< 10$ mK). The steady state PL spectra were collected using a home-built confocal micro-PL set up as described in previous publications [3]. The sample was excited using a PHAROS Light Conversion Ltd. Laser (repetition rate of 750 kHz) whose output was directed into an optical parametric amplifier (OPA, TOPAS-Twins, Light Conversion Ltd) to create 580 nm (2.1377 eV) light. This wavelength was chosen to selectively excite the $WS_2$ and minimise Tc emission, as shown in the inset of Fig. S1 (b), when using 447 nm excitation, Tc emission overpowers that of the charge transfer (CT) exciton in the heterostructure, as no CT peak is present at 1.7 eV. The 580 nm light (fluence of 112 $\mu$Jcm$^{-2}$) was focused using a 40x numerical aperture (NA) 0.6 objective. We have estimated our exciton density using the following equation [4]:

$$N = \frac{\alpha P_f}{E} \tag{1}$$

Where $N$ is the exciton density, $\alpha$ is the absorption coefficient, $P_f$ is the pump fluence and $E$ is the excitation energy. Approximating $\alpha$ using the work of Li *et al* [5] we calculated $N$ to be $\sim 2.7 \times 10^{12}$ cm$^{-2}$ when accounting for the objective efficiency of 60%. This low $N$ does not permit biexciton formation.

The sample emission was collected using the same objective and later dispersed and detected using an Andor Technology monochromator and thermoelectric-cooled charge-coupled device. The lifetime measurements included in Fig. S4 were collected using a single photon avalanche diode (Pico-Quant, PDM series) and a single photon counting module (Pico-Quant) with a time resolution of $\sim 100$ ps.

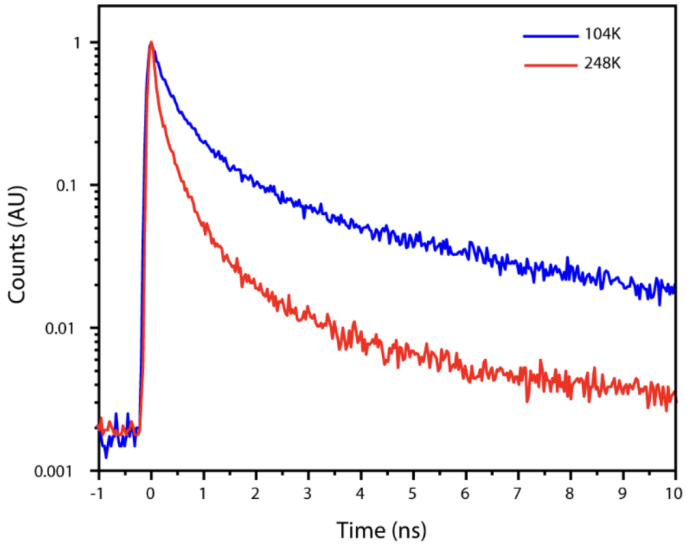


Figure S4. Lifetime dynamics of the heterostructure excited with 580 nm light at 104 K and 248 K

In addition to the PL data presented in the main text, we performed additional measurements to verify that the observed signatures persist in multiple experiments. For a more direct comparison between the experimental trials, we subtract the background emission to isolate the pertinent features in the PL of the heterostructure. The heterostructure presented in the main text was measured twice (two "trials"). While measuring, we optimized the PL intensity by adjusting both the focus and the laser position on the heterostructure. Fig. S5 and S6 summarize all PL spectra collected during trials 1 and 2 respectively. These figures show that while the PL intensity varies between different areas on the heterostructure, the spectral shape is consistent. For each trial and for each temperature, the spectrum with the greatest number of counts was used for further analysis.

In Fig. S7 (a) we show the results presented in the main text only with background subtraction applied. We can compare this to an additional trial (trial 2), shown in Fig. S7 (b) and we observe good agreement both in the peak intensities and positions.

In Fig. S7 (c), we present double-Gaussian fits of the experimental data shown in (b), supporting the idea that the observed PL spectra can be attributed to an interlayer exciton hK' and a phonon-sideband with Gaussian peaks at 1.67 eV to 1.7 eV. The error bars were derived from the Gaussian fittings. For all temperatures reported in both trials, the error for the peak positions of the hK' and phonon sideband ranged from 0.3-3 meV and 4-10 meV respectively. The peak at 1.7 eV we assign to the hK' exciton while the broader peak at 1.67 eV, we propose is formed from multiple phonon-sidebands at different energy, leading to a broad curve.

In our model, the change in peak intensity with temperature could be attributed to either a change in the relative thermal occupation of these excitons, $N_\mu$, or the broadening of the peaks by increased phonon-scattering. By integrating the area of the

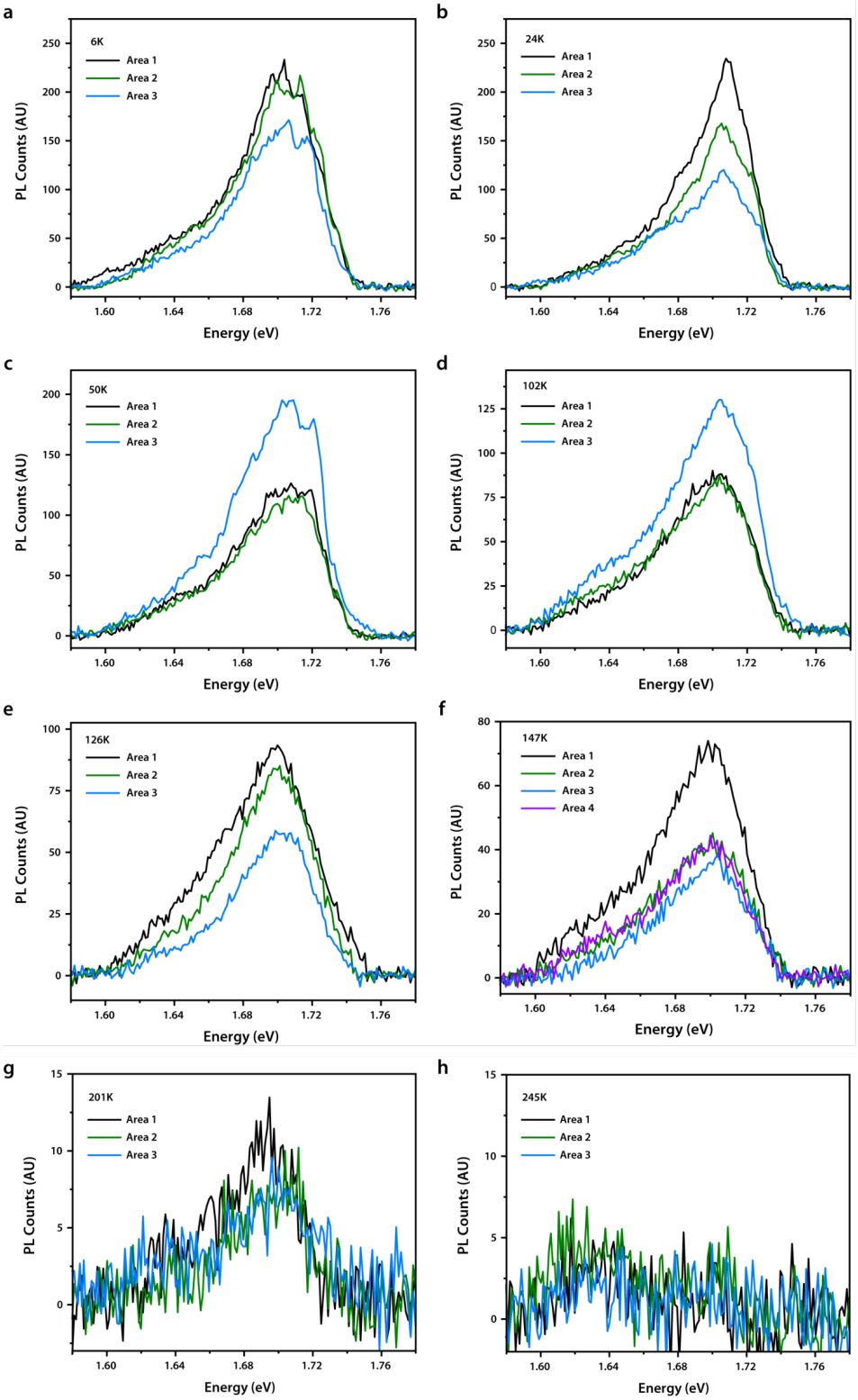


Figure S5. (a-h) PL spectra of all areas measured on the heterostructure during Trial 1.

peaks (as in Fig. S7 (c)), we can attribute the oscillator strength transfer described in the main text to a change in the thermal occupation (as predicted by our model). This is presented in Fig. S7 (d).

Furthermore, the temperature dependent PL was collected for a monolayer of $WS_2$ and pure Tc. In Fig. S8 (a), we display the temperature dependent PL of monolayer $WS_2$ excited with 447 nm light. The inset shows the absence of the interlayer exciton

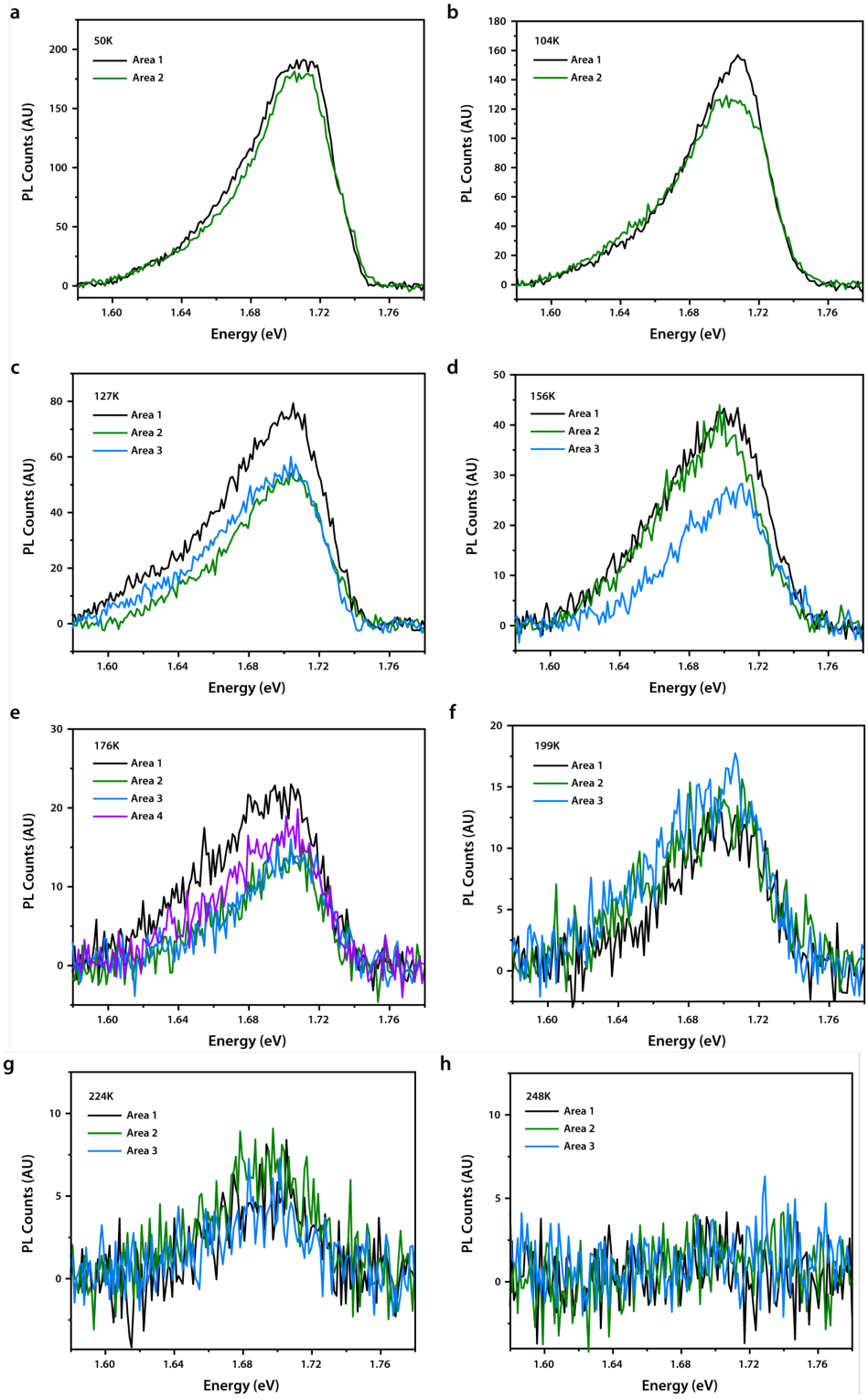


Figure S6. (a-h) PL spectra of all areas measured on the heterostructure during Trial 2.

$hK'$ and phonon-sideband between 1.58-1.78 eV. Likewise, Fig. S8 (b) shows the temperature dependent PL spectrum of pure Tc excited with 580 nm light and also demonstrates the absence of the peaks of interest. This confirms that the signals present in Fig. S7 (a-c) are unique to the heterostructure. Please note that the experimental data presented in this section are from one sample. Data for an adddtion sample are presented in Section IV.

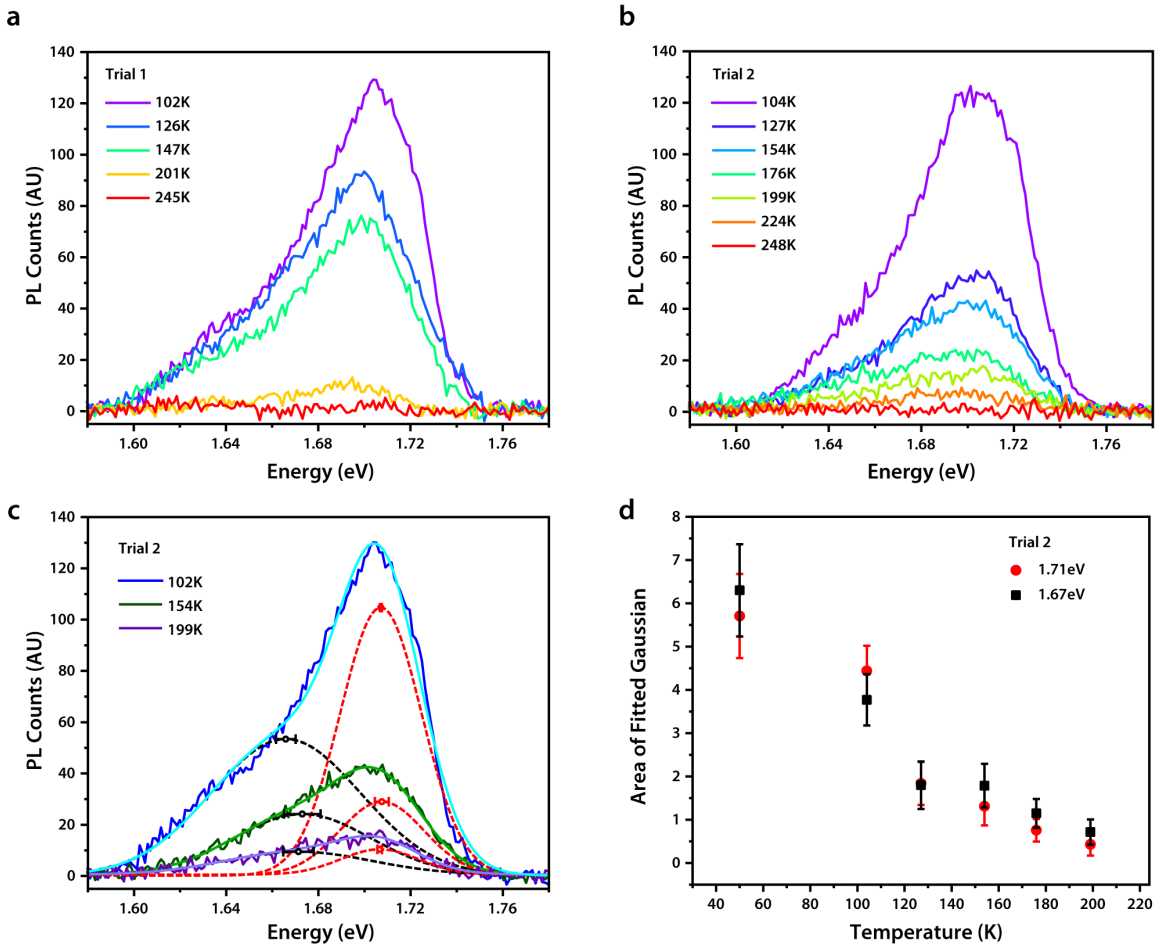


Figure S7. PL spectra following background subtraction for (a) Trial 1 (as shown in main text) and (b) Trial 2, at different temperatures. (c) Double-Gaussian fit of Trial 2 for different temperatures. (d) Temperature dependence of Gaussian fit peaks at 1.67 eV (black) and 1.7 eV (red) presented in (c).

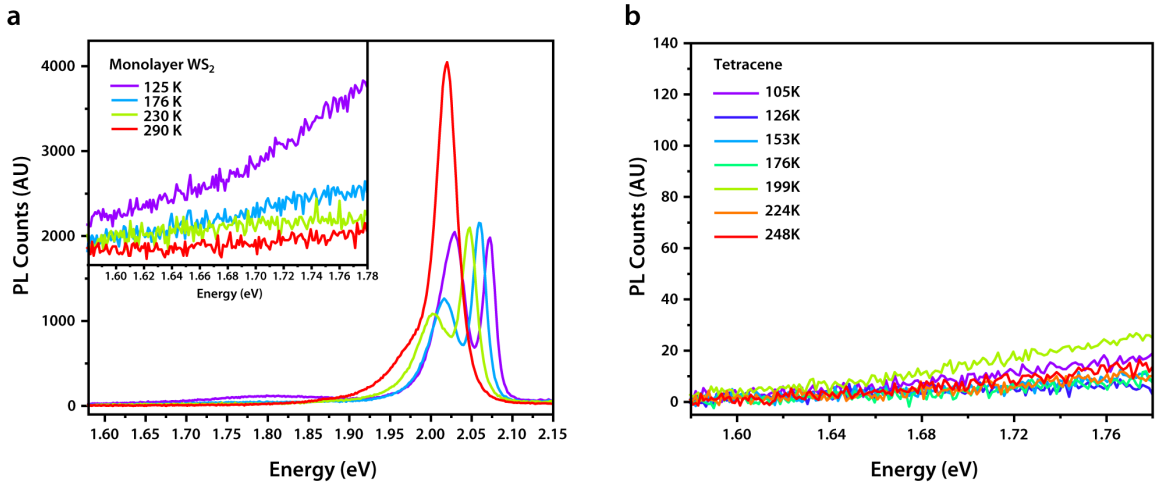


Figure S8. (a) Temperature dependent PL spectra of monolayer $WS_2$ excited with 447 nm light. The inset in (a) is an enlargement of the spectra between 1.58-1.78 eV. (b) Temperature dependent PL spectra of Tc excited with 580 nm light.

## III. CRYOGENIC TEMPERATURES

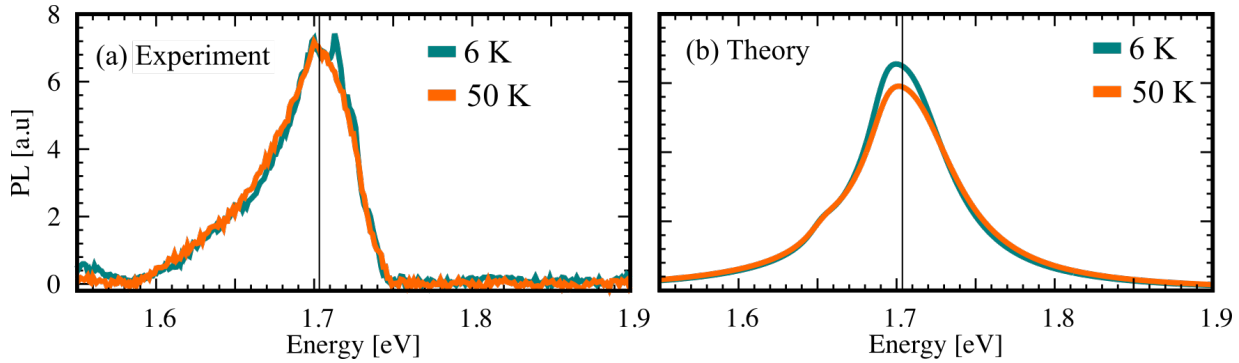


Figure S9. Experimental (a) and theoretical (b) PL spectra of $WS_2$ spectra at low temperatures. Vertical line indicates the energy of the hK' interlayer exciton.

The theory-experiment comparison presented in the main text can be extended to much lower temperatures. In Fig. S9 we compare experimental PL spectra (a) to the theoretical model (b) for 6 K (green) and 50 K (orange). Both temperature curves are qualitatively similar, in both theory and experiment, albeit with slightly increased broadening at 50 K compared to 6 K. The phonon-sideband is still visible at both temperatures. The y-axis scale is the same as presented in Fig 5 of the main text.

## IV. TEMPERATURE AND POWER DEPENDENCE OF AN ADDITIONAL SAMPLE

In order to test the interpretation and reproducibility of our findngs, we fabricated a second $WS_2$/Tc heterostructure sample using the methods outlined in the previous section. In this case the bulk TMD sample was instead purchased from HQ graphene, while the temperature-dependent PL measurements were carried out at a slightly lower pump power ( 78 $\mu$J/cm$^2$).

We find excellent agreement on the temperature dependence between the new sample, Fig. S10, and the sample shown in the main text, with rapid decay of the interlayer exciton PL intensity between 100 and 245 K where it vanishes. This demonstrates the reproducibility of our results.

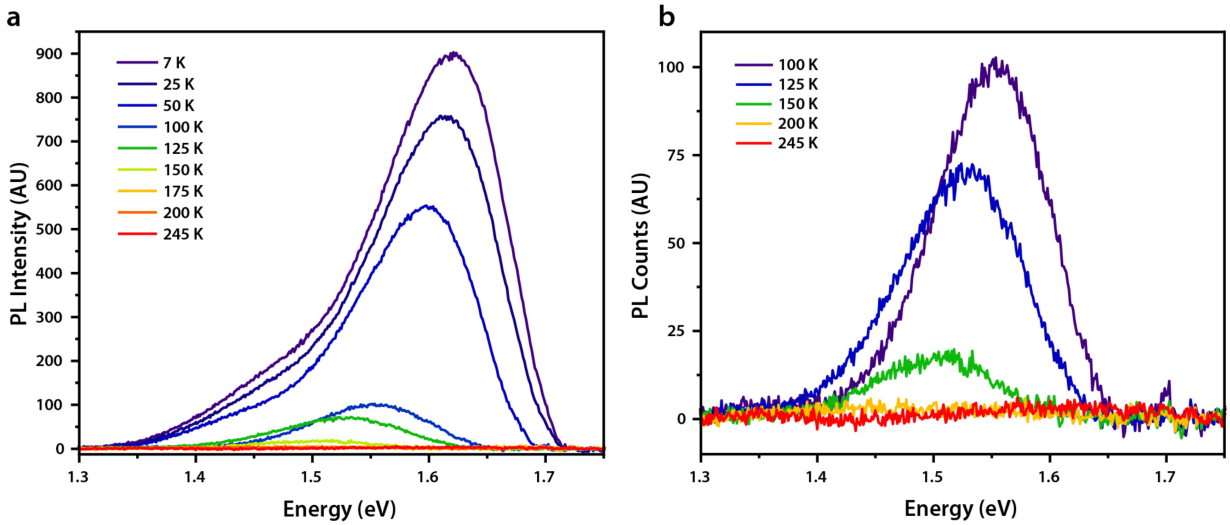


Figure S10. Measurements on second sample (a) Temperature dependence of the second heterostructure's PL spectra with background removed. (b) Temperature dependence at select temperatures of the second heterostructure's PL spectra (in the temperature range as those in the main text).

We performed pump-power dependent PL measurements on the sample as shown in Fig. S11 (a), at 7K. We see a clear PL peak at around 1.62 eV, similar to the previous sample (1.7 eV) with the characteristic shoulder originating from the phonon-sideband contribution. As the pump power increases we see an increase in the overall intensity, however the emission profile shape remains unchanged. This is more clearly seen in Fig. S11(b) where the intensity is normalised. This is consistent with our interpretation that the emission peaks originate from excitons and not trions or defect states. Previous studies have predicted a saturation of interlayer excitons in TMD heterostructures [6] owing to the competition between the interlayer charge-transfer and the long lifetime of the interlayer excitons. Since the lifetime is long the exciton population rapidly builds up and saturation is observed. In contrast, the larger interlayer separation between the Tc and TMD layer leads to a less efficient charge transfer, meaning that this saturation is expected to occur at larger pump powers. Furthermore, as discussed above, our experimental Tc sample is actually composed of several layers of Tc, hence the charges that transfer from the TMD to the interface layers can then hop to the other Tc layers. This also explains the absence of the saturation effect in our results. The linear increase in the integrated PL as a function of pump-fluence (c.f. Fig. S11(c) ) is also strongly indicative of the excitonic origin of our observed PL emission.

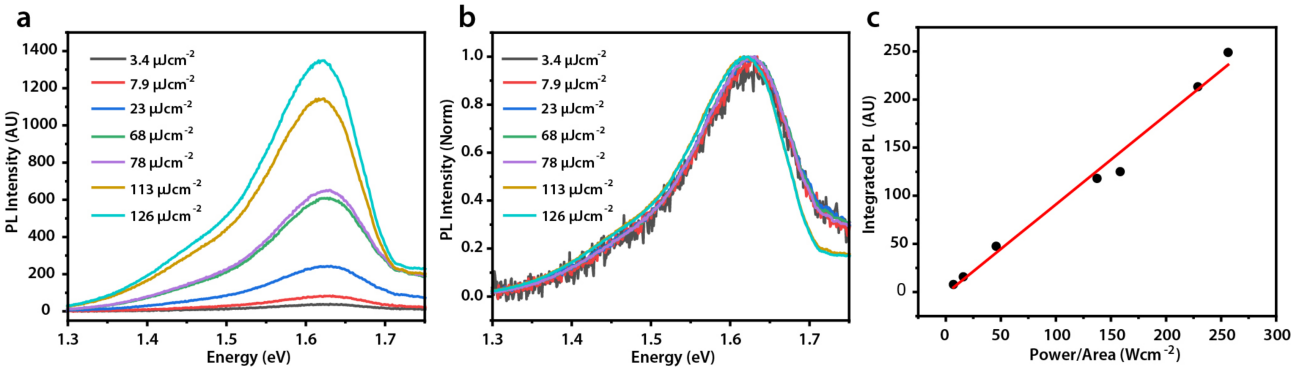


Figure S11. Measurements on second sample. (a) Pump-fluence (power) dependent PL spectra measured at 7 K at frequencies corresponding to the interlayer exciton. (b) Normalized power dependent PL spectra measured at 7 K. (c) Power dependence of the integrated PL measured at 7 K depicting linear behavior.

## V. THEORETICAL MODEL

### A. Wannier Equation

In order to determine the excitonic binding energies and wavefunctions we employ the Wannier equation [7]

$$\left(\frac{\hbar^2\boldsymbol{q}^2}{2m_{ij}^r}+E_{ij}^{\text{Gap}}\right)\varphi_{\boldsymbol{q}}^{ij,\mu}+\sum_{\boldsymbol{k}}V^{ij}(\boldsymbol{k}+\boldsymbol{q})\varphi_{\boldsymbol{k}}^{ij,\mu}=E_{ij,\mu}^{b}\varphi_{\boldsymbol{q}}^{ij,\mu} \tag{2}$$

where $\boldsymbol{q}$ and $\boldsymbol{k}$ are momenta and $E_{ij}^{\text{Gap}}$ is the band gap energy between an electron in layer/valley $i$ and hole in layer/valley $j$. In this equation we also have the reduced mass $m_{ij}^r = m_i^e m_j^h/(m_i^e+m_j^h)$ and the screened Coulomb interaction $V^{ij}(\boldsymbol{k}+\boldsymbol{q})$ between the electron and hole which varies for inter/intra- layer interaction [8]. The excitonic wavefunction is $\varphi_{\boldsymbol{q}}^{ij,\mu}$ where $\mu$ signifies the excitonic energy level, resembling those of a hydrogen atom (1s, 2s, 2p etc). In this work we only consider the lowest-lying, optically active 1s exciton states, hence we drop the index $\mu$ and use it to represent the combined indices $\mu=(i,j)$ determining whether an exciton is inter/intralayer as well as the valley indices. $E_{ij,\mu}^b$ are the corresponding binding energies.

### B. Elliot Formula

In this section we aim to outline the origin of the excitonic Elliot formula in a TMD/Tc heterostructure within our density matrix formalism. The PL intensity can be described using the time evolution of the photon number, $I_{\text{PL}}(\omega_q)=\omega_q\frac{\partial}{\partial t}n_q\propto S_{\mathbf{Q}}^{\mu}$ with the number of emitted photons $n_q=\langle c_q^\dagger c_q\rangle$ and the photon-assisted polarization $S_{\mathbf{Q}}^{\mu}=\sum_q\varphi_{\mathbf{q}}^{\mu *}S_{\mathbf{qQ}}^{vc}$ with $S_{\mathbf{k_1k_2}}^{vc}(t)=\langle c_q^\dagger a_{\mathbf{k_1}}^{\dagger v}a_{\mathbf{k_2}}^{c}\rangle$ [9]. This microscopic quantity describes optically induced transitions from an initial state $(v,\boldsymbol{k_1})$ to a final state $(c,\boldsymbol{k_2})$ under annihilation (creation) of a photon $c_q^{(\dagger)}$. Here, $\mathbf{k_i}$ is the electronic momentum and $\lambda=v,c$ the band index denoting the valence or conduction band, respectively.

Next, we exploit the Heisenberg equation of motion $i\hbar\dot{S}_{\mathbf{Q}}^{\mu}(t)=[H,S_{\mathbf{Q}}^{\mu}(t)]$ [10] to obtain the temporal evolution of the photon-assisted polarization. The Hamilton operator $H=H_0+H_{\text{x-phot}}+H_{\text{x-phon}}+H_{\text{x-tunn}}$ includes the interaction-free part for excitons, photons and phonons $H_0$, the exciton-photon interaction $H_{\text{x-phot}}$ including the optical matrix element $M_Q^{i\sigma}$, and the exciton-phonon coupling $H_{\text{x-phon}}$. The crucial contribution to the Hamilton operator in this work is the tunneling part $H_{\text{tunn}}=\sum_{QQ',ij}T_{QQ'}^{ij}X_Q^{\dagger i}X_{Q-Q'}^{j}$ describing the charge transfer between the layers. The appearing tunneling matrix element $T_{QQ'}^{ij}=\sum_q\varphi_{q+\alpha Q}^{i}t_{QQ'}^{ij}\varphi_{q-\beta Q'}^{j}$ is determined by the overlap of Bloch waves $\Psi_i$ with a tunneling potential $V_{\text{tun}}$, i.e. $t^{ij}=\langle\Psi_i|V_{\text{tun}}|\Psi_j\rangle$. We separate the potential into an in-plane disorder part and out-of-plane part, which is only non-zero between the layers [8]. Then, we can write $t^{ij}=V_{in}(|k_j-k_i|)V_{out}\langle u^i|u^j\rangle_{uc}$ with $u^i$ the lattice periodic parts of the Bloch waves integrated over a unit cell. This integral determines the tunneling strength and we assume a typical value of 0.01 known from TMD/TMD heterostructures [8]. The remaining in-plane disorder potential can be estimated via a disorder potential with correlation length in the order of the exciton Bohr radius.

In a last step, we project into a new basis where the tunneling part of the Hamiltonian is included in an effective single-particle

Hamiltonian, i.e.

$$H_0 + H_{\text{x-tun}} = \sum_{Q,i} \epsilon^i_Q X^{\dagger i}_Q X^i_Q + \sum_{QQ',ij} T^{ij}_{QQ'} X^{\dagger i}_Q X^j_{Q-Q'} = \sum_{\mu Q} \mathcal{E}_{\mu Q} \tilde{X}^\dagger_{\mu Q} \tilde{X}_{\mu Q}. \tag{3}$$

Note that for the applied transformation $\hat{U}_\mu$, we exploited $\tilde{X}^\dagger_{\mu Q} = \hat{U}_\mu X^\dagger_{\mu Q} = \sum_j U^j_{\mu Q} X^{j\dagger}_Q$ and $\hat{U}^\dagger_\mu \hat{U}_\mu = \mathcal{I}$, i.e. a uniform transformation. As intra- and interlayer states are off-resonant and we do not include hybridization effects, eigenenergies are not affected by this transformation. Solving Heisenberg's equations of motion in this excitonic tunnelling basis, we finally arrive at the Elliot formula for the phonon assisted polarisation $I^b_{\text{PL}}$ for intra- and interlayer excitons [9]

$$I_{\text{PL}}(\omega, T) \propto \sum_{\mu = \text{ KK,hK}} \frac{|M_\mu|^2 \gamma_\mu N_\mu(T)}{(E_\mu - \omega)^2 + (\gamma_\mu + \Gamma_\mu(T))^2}, \tag{4}$$

with terms described in the main text.

### C. Energy Landscape and Screening Parameters

To calculate the appearing matrix elements in the Hamilton operator, we apply a nearest-neighbor tight-binding approach [7, 10, 11] which includes fixed (not adjustable) input parameters (effective masses, band gap energies, cf. Table S2) from DFT calculations for the electronic bandstructure [12, 13].

| energies for state $\mu$ | | | | | | | | | | | | |
|---|---|---|---|---|---|---|---|---|---|---|---|---|
| | KK | | hK | | hK' | | hΛ | | Kl | | hl | |
| $E_\mu^g$ | 2.18 | | 2.01 | | 1.98 | | 2.03 | | 3.4 | | 3.0 | |
| $E_\mu^b$ | 196 | | 243 | | 272 | | 328 | | 272 | | 440 | |
| $E_\mu$ | 2.00 | | 1.76 | | 1.705 | | 1.71 | | 3.12 | | 2.56 | |
| screening parameters | | | | | | | electronic masses | | | | | |
| $\epsilon^{\text{TMD}}$ | $\epsilon^{\text{Tc}}$ | $\epsilon^{\text{sur}}$ | $d^{\text{TMD}}$ | $d^{\text{Tc}}$ | $d^{\text{TMD-Tc}}$ | $m_K^c$ | $m_\Lambda^c$ | $m_{K'}^c$ | $m_K^v$ | $m^h$ | $m^l$ | |
| 13.61 | 3.69 | 2.45 | 0.61 | 1.1 | 0.3 | 0.27 | 0.64 | 0.36 | 0.36 | 3.0 | 6.7 | |

Table S1. **Energy Landscape and screening parameters.** Electronic band gap energies $E_\mu^g$ (in eV, from [3, 12]), calculated exciton binding energies $E_\mu^b$ (meV) and spectral position $E_\mu$ (eV) for intra- and interlayer excitons, screening parameters for dielectric environment $\epsilon$ (from [14, 15]) and thickness $d$ (in nm, from [14, 16]) and electronic masses (in $m_0$, from [12, 17]). All values refer to a $WS_2$/Tc heterostructure on an $SiO_2$ substrate.

## VI. PENTACENE/MOS$_2$

In order to demonstrate the scope and generality of our model we calculate the PL spectrum for a pentacene/$MoS_2$ heterostructure. Such a structure has previously been fabricated by Bettis-Homan et al. [18], and is predicted to be type-II, playing host to interlayer excitons.

The band alignment and other input parameters are obtained from the literature and are shown in Table S2. We find that, owing to the smaller separation between the conduction band of $MoS_2$ and the HOMO of pentacene, the interlayer exciton lies around 1.35 eV below the bright intralayer excitons KK and hl (c.f Table S2). We find that this significant energy separation will lead to dominant signal from the interlayer exciton in the temperature range 0 - 300 K as seen in Fig S12 (a). Clearly the dominant signal arrises from the hK exciton and not the KK even at room temperatures. In this system we also recover the phonon-sideband, which can be clearly seen as a pronounced shoulder at 50 K in Fig. S12 (b). At larger temperatures this sideband is no longer visible owing to the increased thermal broadening of the PL spectra. These results demonstrate the generality of our model, which is able to describe the PL spectra of general organic/TMD systems.

| energies for state $\mu$ | | | | | | | | | | | | |
|---|---|---|---|---|---|---|---|---|---|---|---|---|
| | KK | | hK | | hK' | | hΛ | | Kl | | hl | |
| $E_\mu^g$ | 2.5 | | 1.2 | | 1.2 | | 1.2 | | 3.7 | | 2.7 | |
| $E_\mu^b$ | 240 | | 285 | | 291 | | 337 | | 310 | | 410 | |
| $E_\mu$ | 2.26 | | 0.91 | | 0.92 | | 1.11 | | 3.39 | | 2.29 | |
| screening parameters | | | | | | | electronic masses | | | | | |
| $\epsilon^{\text{TMD}}$ | $\epsilon^{\text{Tc}}$ | $\epsilon^{\text{sur}}$ | $d^{\text{TMD}}$ | $d^{\text{Tc}}$ | $d^{\text{TMD-Tc}}$ | $m_K^c$ | $m_\Lambda^c$ | $m_{K'}^c$ | $m_K^v$ | $m^h$ | $m^l$ | |
| 15.1 | 3.6 | 2.45 | 0.61 | 1.1 | 0.3 | 0.43 | 0.46 | 0.77 | 0.54 | 2.2 | 2.55 | |

Table S2. **Energy Landscape and screening parameters.** Electronic band gap energies $E_\mu^g$ (in eV, from [12, 18]), calculated exciton binding energies $E_\mu^b$ (meV) and spectral position $E_\mu$ (eV) for intra- and interlayer excitons, screening parameters for dielectric environment $\epsilon$ (from [14, 19]) and thickness $d$ (in nm, from [14, 20]) and electronic masses (in $m_0$, from [12, 21]). All values refer to a $MoS_2$/Pc heterostructure on an $SiO_2$ substrate.


[1] Y. Huang, E. Sutter, N. N. Shi, J. Zheng, T. Yang, D. Englund, H.-J. Gao, and P. Sutter, ACS Nano **9**, 10612 (2015).
[2] D. H. Arias, J. L. Ryerson, J. D. Cook, N. H. Damrauer, and J. C. Johnson, Chemical science **7**, 1185 (2016).
[3] T. Zhu, L. Yuan, Y. Zhao, M. Zhou, Y. Wan, J. Mei, and L. Huang, Science Advances **4**, 3104 (2018).
[4] L. Yuan, B. Zheng, J. Kunstmann, T. Brumme, A. B. Kuc, C. Ma, S. Deng, D. Blach, A. Pan, and L. Huang, Nature materials **19**, 617 (2020).
[5] Y. Li, A. Chernikov, X. Zhang, A. Rigosi, H. M. Hill, A. M. Van Der Zande, D. A. Chenet, E.-M. Shih, J. Hone, and T. F. Heinz, Physical Review B **90**, 205422 (2014).

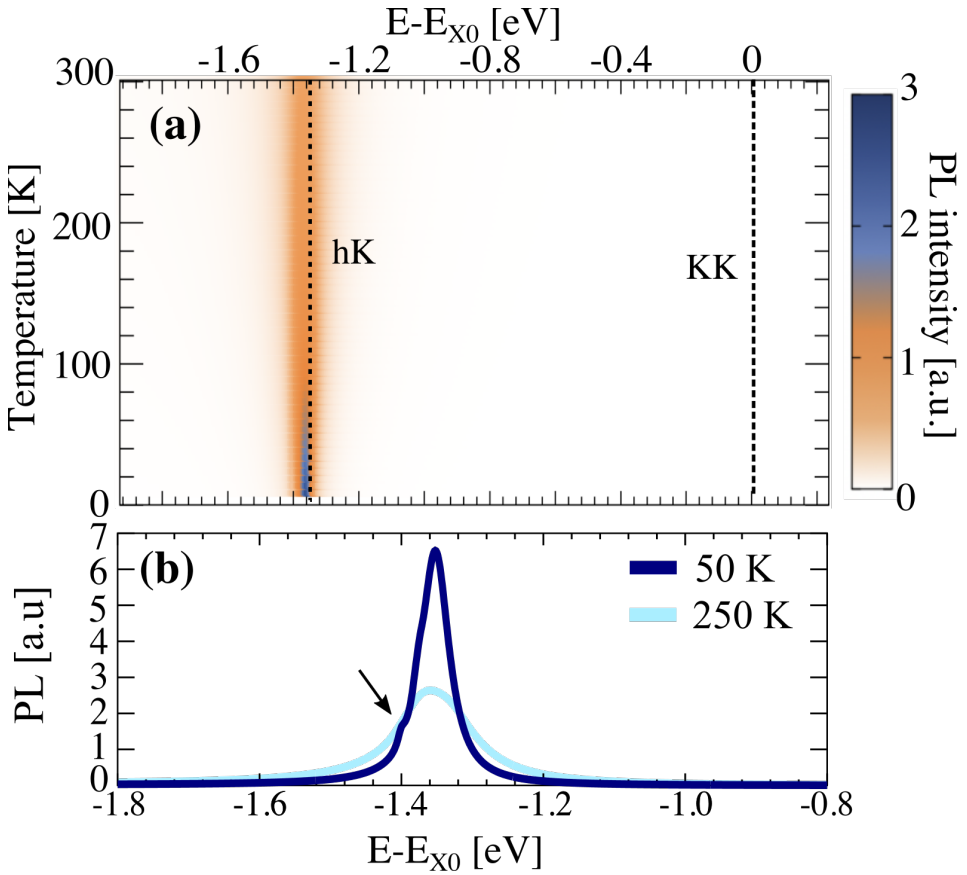


Figure S12. (a) PL spectra as a function of temperature, with x-axis shifted relative to the intralayer exciton energy. Bright intralayer exciton KK and dominant interlayer exciton hK energies are marked with dashed lines. (b) PL cuts at 50 K (dark blue) and 250 K (light blue). Phonon sideband is marked with an arrow.


[6] P. Rivera, J. R. Schaibley, A. M. Jones, J. S. Ross, S. Wu, G. Aivazian, P. Klement, K. Seyler, G. Clark, N. J. Ghimire, *et al.*, Nature communications **6**, 1 (2015).
[7] M. Kira and S. Koch, Progress in Quantum Electronics **30**, 155 (2006).
[8] S. Ovesen, S. Brem, C. Linderälv, M. Kuisma, T. Korn, P. Erhart, M. Selig, and E. Malic, Communications Physics **2**, 1 (2019).
[9] S. Brem, A. Ekman, D. Christiansen, F. Katsch, M. Selig, C. Robert, X. Marie, B. Urbaszek, A. Knorr, and E. Malic, Nano Letters **20**, 2849 (2020).
[10] H. Haug and S. W. Koch, *Quantum theory of the optical and electronic properties of semiconductors* (World Scientific Publishing Company, 2009).
[11] E. Malic, A. Setaro, P. Bluemmel, C. F. Sanz-Navarro, P. Ordejón, S. Reich, and A. Knorr, Journal of Physics: Condensed Matter **24**, 394006 (2012).
[12] A. Kormanyos, G. Burkard, M. Gmitra, J. Fabian, V. Zolyomi, N. D. Drummond, and V. Falko, 2D Materials **2**, 022001 (2015).
[13] T. Breuer, T. Maßmeyer, A. Mänz, S. Zoerb, B. Harbrecht, and G. Witte, physica status solidi (RRL)–Rapid Research Letters **10**, 905 (2016).
[14] A. Laturia, M. L. Van de Put, and W. G. Vandenberghe, npj 2D Materials and Applications **2**, 1 (2018).
[15] O. Leenaerts, B. Partoens, and F. Peeters, Physical Review B **77**, 125416 (2008).
[16] X.-Y. Xie, X.-Y. Liu, Q. Fang, W.-H. Fang, and G. Cui, The Journal of Physical Chemistry A **123**, 7693 (2019).
[17] K. Doi, K. Yoshida, H. Nakano, A. Tachibana, T. Tanabe, Y. Kojima, and K. Okazaki, Journal of applied physics **98**, 113709 (2005).
[18] S. Bettis Homan, V. K. Sangwan, I. Balla, H. Bergeron, E. A. Weiss, and M. C. Hersam, Nano letters **17**, 164 (2017).
[19] S. Refaely-Abramson, S. Sharifzadeh, M. Jain, R. Baer, J. B. Neaton, and L. Kronik, Physical Review B **88**, 081204 (2013).
[20] C. Cocchi, T. Breuer, G. Witte, and C. Draxl, Physical Chemistry Chemical Physics **20**, 29724 (2018).
[21] V. Coropceanu, Y. Li, Y. Yi, L. Zhu, and J.-L. Brédas, MRS bulletin **38**, 57 (2013).